Three-dimensional effect of particle motion on plasma filament dynamics

Cite as: Phys. Plasmas **26**, 062104 (2019); https://doi.org/10.1063/1.5093561
Submitted: 21 February 2019 • Accepted: 09 May 2019 • Published Online: 04 June 2019

Hiroki Hasegawa and Seiji Ishiguro

Physics of Plasmas ARTICLE scitation.org/journal/php

Three-dimensional effect of particle motion on plasma filament dynamics

Cite as: Phys. Plasmas **26**, 062104 (2019); doi: 10.1063/1.5093561
Submitted: 21 February 2019 · Accepted: 9 May 2019 ·
Published Online: 4 June 2019

Hiroki Hasegawa[1,2] and Seiji Ishiguro[1,2]

AFFILIATIONS

[1]Department of Helical Plasma Research, National Institute for Fusion Science, National Institutes of Natural Sciences, Toki 509-5292, Japan
[2]Department of Fusion Science, SOKENDAI (The Graduate University for Advanced Studies), Toki 509-5292, Japan

ABSTRACT

It is shown for the first time with the three-dimensional (3D) electrostatic particle-in-cell simulation that the plasma particle motion influences plasma filament dynamics three-dimensionally. If we assume that the filament size on the cross section is a few times as large as $\rho_e\sqrt{m_i/m_e}$ and that the ion temperature is higher than the electron temperature, the poloidal symmetry of filament propagation is broken and the propagation velocity has the non-negligible poloidal component, where ρ_e is the electron Larmor radius. Then, it is observed that such propagation dynamics depend on the position on the magnetic field line, i.e., in the toroidal direction. As the ion temperature increases beyond the electron temperature, the perpendicular electric field in a filament varies greatly according to the toroidal position. Such a variation might arise from the presheath potential drop on the potential hill side in a filament. Thus, the toroidal dependence of the propagation dynamics appears.

I. INTRODUCTION

The plasma filament aligned with the magnetic field line is a universal structure in astrophysical, space, and laboratory plasmas. For instance, filamentary structures have been observed with the flux tubes on the surface of the Sun.[1] Also, it has been reported that such a coherent structure is intermittently formed and transported across magnetic field lines in the boundary layer plasma in many magnetic confinement devices,[2–9] where these structures are called "blob" or "hole" in fusion plasmas. The dynamics of plasma filaments have been investigated on the basis of fluid models [e.g., magnetohydrodynamics (MHD) equations[1] and various types of sets of the vorticity, continuity, and other equations[2,3,10–12]] in most of the numerical studies. Furthermore, the ion temperature or kinetic effects on the filament dynamics have been considered in some recent works for the fusion boundary layer plasmas and are thought to break a poloidal symmetry of filament propagation.[13–20] However, investigations of the three-dimensional kinetic effects on the filament phenomena with considering full kinetic dynamics of plasma particles have not been conducted.

On the other hand, in order to study the kinetic dynamics on the filament phenomena, which are disregarded or are assumed to be described by certain parameters derived from simple models in conventional fluid equations, we have developed the three-dimensional (3D) electrostatic particle-in-cell (PIC) simulation code[21–23] called "p3bd" code. The p3bd code simulates self-consistently the full electron and ion dynamics in the phenomena without restriction on or disregard for various quantities, dynamics, and situations, e.g., the ion temperature (Larmor radius), the dynamics (spatial variation) parallel to the magnetic field, the sheath dynamics on conductive plates, the large deviation of the velocity distribution from the Maxwellian, and the situation where the drift approximation is not satisfied. We have shown that the p3bd code reproduces the self-consistent current system in a filament with the sheath on conductive end plates.[24] We have found the temperature structure in a filament[24] and the impurity ion transport by plasma filaments[25,26] with the p3bd code.

In this paper, we investigate the three-dimensional effect of particle motion on plasma filament dynamics by means of the 3D-PIC code. In Sec. II, we briefly mention the configuration and parameters of the 3D-PIC simulation. In Sec. III, we show results of the 3D-PIC simulation. The simulations confirm that the poloidal symmetry breaking is reproduced even if the issues mentioned above are not restricted and show that the plasma particle motion influences the plasma filament dynamics three-dimensionally. Finally, we give a summary of our work and offer discussion in Sec. IV.

II. SIMULATION METHOD

In the p3bd code, the full dynamics (including the Larmor motion) of electron and ion particles which compose both filamentary

and background plasmas are computed by the equation of motion and the self-consistent electric field formed by the charge density which is obtained from all plasma particles and are solved with Poisson's equation.[27] The simulation system is set as a slab geometry with x (the counter radial direction), y (the poloidal direction), and z (the toroidal direction parallel to the magnetic field $\boldsymbol{B}$) as shown in Fig. 1. The external magnetic field strength B is given by $B(x) = 2L_xB_{Lx}/(3L_x - x)$, where L_x, L_y, and L_z are the system size in the x, y, and z directions and B_{Lx} is the magnetic field strength at $x = L_x$. Thus, B has a gradient in the x direction. A plasma filament structure is initially placed as a cylindrical shape which reaches to both end plates and is parallel to the magnetic field. Therefore, a filament moves in the $-x$ direction because of this configuration. The method to distribute plasma particles in the simulation system was described in detail in the previous papers.[23,24] The boundary conditions are as follows. In the x direction, the particle absorbing boundary condition is applied at $x = 0$ (corresponding to a conductive wall) where the electric potential is given as $\phi = 0$ and the reflecting boundary condition is used at $x = L_x$ where $\partial\phi/\partial x = 0$. In the y direction, the periodic boundary condition is applied. In the z direction, the particle absorbing boundary condition is applied at both edges, $z = 0$ and L_z (corresponding to conductive end plates), where $\phi = 0$. In the simulation, the Debye sheath is formed self-consistently without artificial sheath models since the grid size is equal to the Debye length. Thus, a sheath current boundary condition which is usually used in other simulations of boundary layer plasma is not applied. Therefore, the parallel current including current near the end plates is self-consistently simulated in the code.

The simulation parameters are as follows. The system size is $L_x \times L_y \times L_z = 61.97\,\rho_s \times 61.97\,\rho_s \times 7931.87\,\rho_s$ and the grid spacing is $\Delta_g = 0.9683\,\rho_s$, where $\rho_s = c_s/\Omega_i$, c_s is the ion acoustic speed for a cold ion plasma, i.e., $c_s = \sqrt{T_e/m_i}$, Ω_i is the ion cyclotron frequency at $x = L_x$, T_e is the initial electron temperature, and m_i is the ion mass. The time step width is $\Delta t = 2.421 \times 10^{-3}\,\Omega_i^{-1}$. There are 64 electrons and an equal number of ions per cell on average. The ion-to-electron mass and charge ratios are $m_i/m_e = 100$ and $q_i/|q_e| = 1$, respectively. Thus, $\rho_s = \rho_e\sqrt{m_i/m_e}$, where ρ_e is the electron Larmor radius. The external magnetic field strength is set as $\Omega_i/\omega_{pi} = 1$, where ω_{pi} is the ion plasma frequency in the background plasma. The initial density ratio of the filament to the background plasma is $n_{f0}/n_0 = 2.7$. The initial filament size in the poloidal cross-section is $\delta_f = 3.87\rho_s$. The initial position of the filament is $(x_{f0}, y_{f0}) = (3L_x/4, L_y/2)$. We have carried out the three cases in which the initial ion-to-electron thermal velocity ratios are given by $v_{Ti}/v_{Te} = 0.05$, 0.10, and 0.20, respectively. That is, the initial ion-to-electron temperature ratios and the initial ion Larmor radii are $T_i/T_e = 0.25$, 1.00, and 4.00 and $\rho_i/\rho_s = 0.5$, 1.0, and 2.0. The configuration and the parameters described above indicate that a filament in the simulations exists in the sheath-connected regime[2,28] since collisionless plasma is assumed. Also, in this study, δ_*, which is the particular filament width for the long distance movement caused by the situation in which the inertial term, the driving term, and the dissipation term are comparable with each other,[2] is given by $\delta_*/\rho_s \approx [L_z^2/(\rho_s L_x)]^{1/5} \approx 16$. Thus, the inertial term caused by the polarization drift current dominates in the blob dynamics since $\delta_f < \delta_*$, that is, the blobs are in the "inertial" regime.

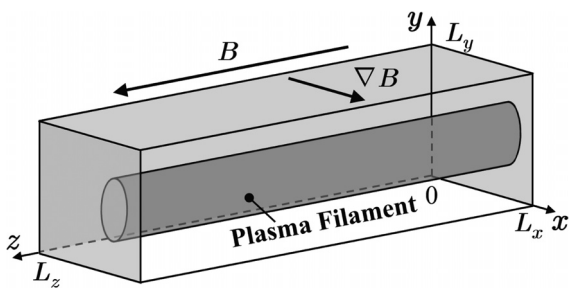

FIG. 1. Configuration of the simulation.

III. SIMULATION RESULTS

A. Toroidal dependence of filament dynamics

Figure 2 shows the electron density distributions in the low (a) and high (b) ion temperature cases at $t = 145.24\,\Omega_i^{-1}$ when the filament has moved for more than $10\rho_s$ in the radial direction after the formation of the self-consistent potential structure in the filament. As seen in Fig. 2(a), in the low ion temperature case, the filament propagates while maintaining the poloidal symmetry. On the other hand, Fig. 2(b) indicates that the poloidal symmetry of propagation of the filament is broken in the high ion temperature case and that the profile of the filament on each poloidal cross section shown in the figure differs from each other. That is, the propagation dynamics have the toroidal dependence in the high ion temperature case.

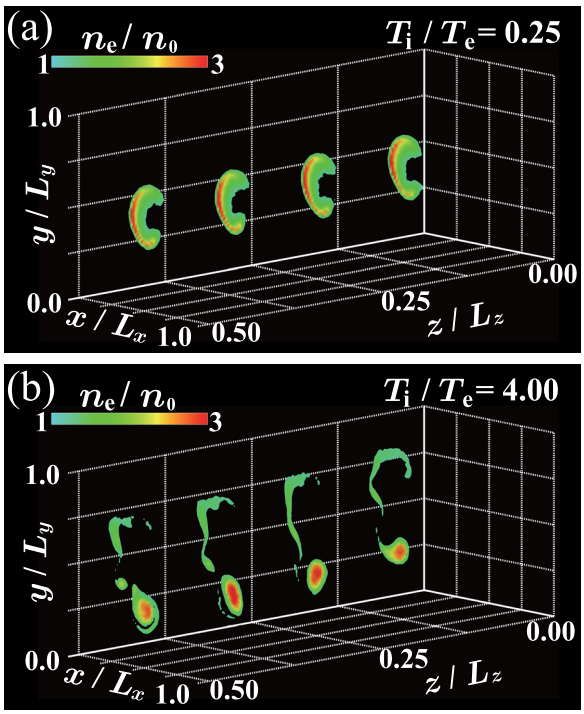

FIG. 2. Electron density distributions in the low (a) and high (b) ion temperature cases at $t = 145.24\,\Omega_i^{-1}$, where the ion temperatures in the panels (a) and (b) are $T_i/T_e = 0.25$ and 4.00, respectively. Four color contours in each panel show the electron density distributions in the filament on the x–y planes at $z/L_z = 0.125$, 0.25, 0.375, and 0.5, respectively.

In order to prove the toroidal dependence quantitatively, we have analyzed the time evolution of the position of the center of electron mass in the filament on each poloidal cross-section as shown in Fig. 3, which describes approximately the movement of the filament. In Fig. 3, it is found that the radial propagation speed becomes faster with increasing T_i [see panels (a), (c), and (e)] as the observed speeds for each case at $z/L_z = 0.5$ are $v_{fx}/c_s = 0.15$, 0.20, and 0.27. Here, the observed speed is calculated from the observed position of the center of electron mass in the filament for a certain time length which is $80 < \Omega_i\, t < 130$ for $T_i/T_e = 0.25$, $70 < \Omega_i\, t < 100$ for $T_i/T_e = 1.00$, or $40 < \Omega_i\, t < 70$ for $T_i/T_e = 4.00$. It is also noted that the observed speeds are nearly proportional to $(1 + T_i/T_e)^{1/2}$. This relation is expected by the scaling law of blob velocity for finite ion temperature in the inertial regime shown by Eq. (28) in Ref. 17, Eq. (9) in Ref. 18, and Eq. (33) in Ref. 23.

Furthermore, as T_i increases, the poloidal displacement and the difference among the poloidal displacements on each poloidal cross-section become larger [see panels (b), (d), and (f)]. The large difference among the poloidal displacements on each poloidal cross-section shows quantitatively the toroidal dependence of filament propagation dynamics in the high T_i cases. Also, in the high T_i cases, the collapse of the filament shape by the poloidal symmetry breaking as shown in Fig. 2(b) may prevent the filament from moving in the radial direction after the filament propagates for more than $10\rho_s$ as Figs. 3(c) and 3(e) indicate.

B. Three-dimensional structure of the electric field

The toroidal dependence of the poloidal filament movement, which is mentioned in Sec. III A, arises from the toroidal dependence of the electric field. In order to prove that, the structure of the electric field in the filament is analyzed as shown in Figs. 4 and 5 which represent the distribution of the strength of the electric field perpendicular to the z direction, $|\boldsymbol{E}_\perp|$, on four poloidal cross-sections for the low and high T_i cases and the relation between z and the maximum of $|\boldsymbol{E}_\perp|$ in the filament, respectively.

1. Unbalanced dipole potential structure

Figure 4 indicates that the area in which the perpendicular electric field in the filament is intense moves to the deepest point in the potential well as T_i increases and that the perpendicular electric field strength in the intense $|\boldsymbol{E}_\perp|$ area becomes larger in the high T_i case than in the low T_i case. The movement of the intense $|\boldsymbol{E}_\perp|$ area is also revealed by the concentration of the white contour lines for the electric potential near the deepest point in the potential well in Fig. 4(b). Furthermore, although the observed radial propagation speeds are nearly proportional to $(1 + T_i/T_e)^{1/2}$ as mentioned in Sec. III A, the values of $|\boldsymbol{E}_\perp|$ at $z/L_z = 0.5$ have no linear relation with $(1 + T_i/T_e)^{1/2}$ as seen from Fig. 5. This means that the intense $|\boldsymbol{E}_\perp|$ area is localized more intensively in the high T_i case than in the low T_i case. These facts prove that the depth and width of the potential well formed by the

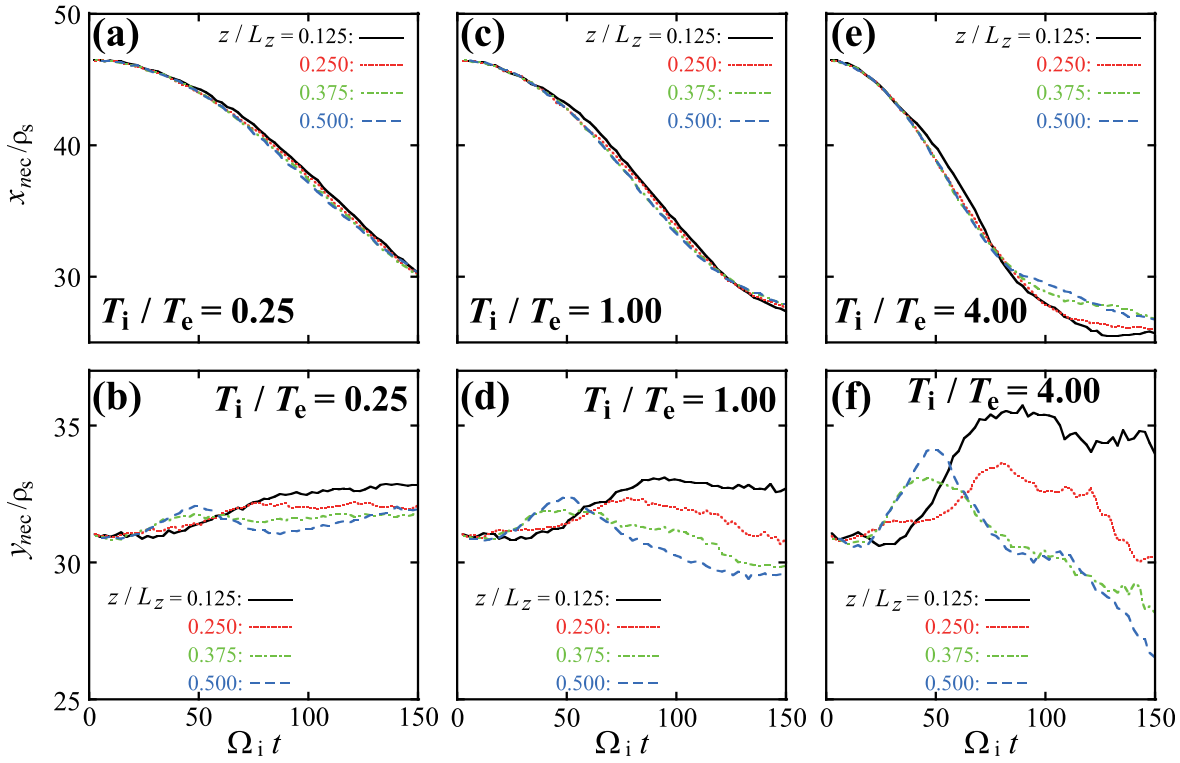

FIG. 3. Time evolutions of the positions of the centers of electron mass in the filament on the x-y planes at $z/L_z = 0.125$ (black solid lines), 0.25 (red dotted lines), 0.375 (green dashed-dotted lines), and 0.5 (blue broken lines). The top and bottom panels show the time evolutions of the x and y components. The left, middle, and right panels represent the time evolutions when $T_i/T_e = 0.25$, 1.00, and 4.00.

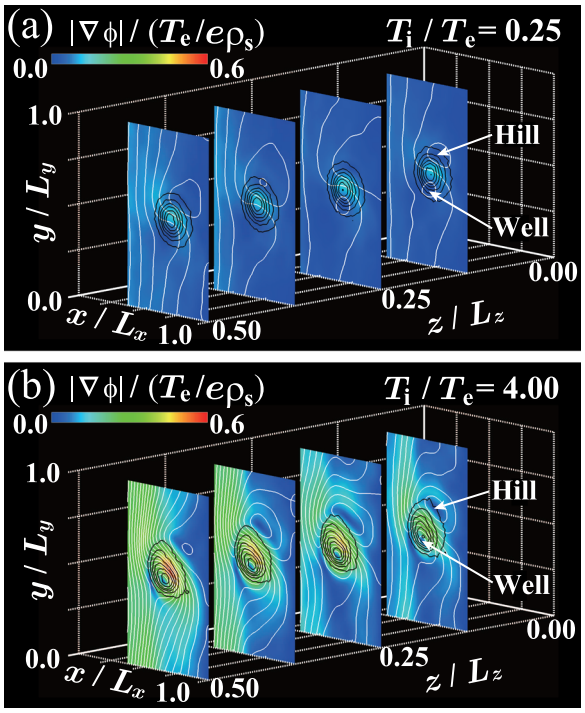

FIG. 4. Distributions of the strength of the perpendicular electric field on four poloidal cross-sections at $z/L_z = 0.125$, 0.25, 0.375, and 0.5 for the low (a) and high (b) T_i cases at $t = 41.15\,\Omega_i^{-1}$. The black and white contour lines represent the electron density distributions and the electric potential distributions, respectively.

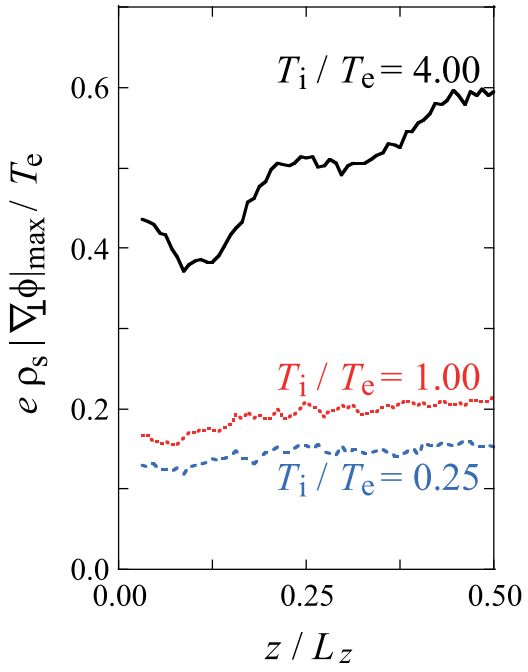

FIG. 5. Relation between z and the maximum of the perpendicular electric field strength in the filament, $|\boldsymbol{E}_\perp|$, at $t = 41.15\,\Omega_i^{-1}$, where the black solid, red dotted, and blue broken lines represent the relations when $T_i/T_e = 4.00$, 1.00, and 0.25, respectively.

negative charges of electrons become larger and narrower than the height and width of the potential hill with increasing T_i. Such an unbalanced dipole potential structure is thought to arise from the effect of the ion Larmor radius which becomes much larger than that for the ion acoustic speed as $\rho_i \gtrsim \rho_e\sqrt{m_i/m_e}$.

On the other hand, from the white contour lines for the electric potential in Fig. 4, it is found that the radial ($-x$) component of the electric field in the filament becomes larger as T_i increases. Such a finite radial component of the electric field causes the considerable motion of the filament in the $+y$ direction at the early stage ($20 < \Omega_i t < 50$) in the high T_i case as shown in Fig. 3(f). However, after that, the center of electron mass in the filament moves in the $-y$ direction because the electric field around the deepest point in the potential well is larger than that around the peak of the potential hill and a greater number of plasma particles rotate around the potential well. The poloidal symmetry breaking occurs due to such an unbalanced dipole potential structure in the filament through the sequence of the processes mentioned above, which are also shown in Ref. 20.

2. Toroidal variation in the electric field

The most important point indicated in Fig. 4 is that the toroidal dependence of $|\boldsymbol{E}_\perp|$ in the high T_i case is stronger than that in the low T_i case. In order to confirm this point clearly, we show the spatial variation of the maximum of the perpendicular electric field strength in the filament in the z direction in Fig. 5. From Fig. 5, it is found that the maximum of $|\boldsymbol{E}_\perp|$ at $z/L_z = 0.125$ reaches only 64% of the maximum of $|\boldsymbol{E}_\perp|$ at $z/L_z = 0.5$.

Such toroidal dependence of the electric field is thought to arise from the large presheath potential drop on the potential hill side in a filament. In order to estimate the presheath potential drop, we have probed the maxima of the electric potential in the filament (i.e., the height at the potential hill) at $z/L_z = 0.5$ and 0.125 at $t = 41.15\,\Omega_i^{-1}$ and calculated the difference between the maxima. As a result, it is obtained that $e\Delta\phi_{max}/T_e = 0.46$, 1.06, and 2.58 for $T_i/T_e = 0.25$, 1.00, and 4.00, respectively, where $\Delta\phi_{max}$ is defined as $\Delta\phi_{max} = \phi_{max}\,(z/L_z = 0.5) - \phi_{max}\,(z/L_z = 0.125)$. On the other hand, the presheath potential drop on the potential well side does not become larger with increasing T_i. The differences of the minimum of the electric potential in the filament (i.e., the differences of the depth at the potential well) between $z/L_z = 0.5$ and 0.125 at $t = 41.15\,\Omega_i^{-1}$ are obtained as $e\Delta\phi_{mim}/T_e = 0.25$, 0.51, and 0.18 for $T_i/T_e = 0.25$, 1.00, and 4.00, respectively, where $\Delta\phi_{min}$ is defined as $\Delta\phi_{min} = \phi_{min}(z/L_z = 0.5) - \phi_{min}(z/L_z = 0.125)$. The dependence of the presheath potential drop on the ion temperature has not been observed on the potential well side, while $\Delta\phi_{max}$ is positively correlated with T_i.

The toroidal variation of $|\boldsymbol{E}_\perp|$ which is induced by the large presheath potential drop on the potential hill side in the high T_i cases causes the toroidal dependence of the poloidal filament movement. As a result, the filament movements in the $+y$ direction in the early stage ($t < 50\,\Omega_i^{-1}$) and the filament movements in the $-y$ direction in the latter stage ($t > 50\,\Omega_i^{-1}$) on each poloidal cross-section, which are represented in Fig. 3, are positively correlated with the maximum of $|\boldsymbol{E}_\perp|$. On the other hand, the reason why the filament continues moving in

the $+y$ direction in the middle stage ($50 < \Omega_i\, t < 80$) on the poloidal cross-sections at $z/L_z = 0.25$ and 0.125 may be that the amount of plasma particles which rotate around the potential well is small due to the potential structure.

IV. SUMMARY AND DISCUSSION

In summary, we have reported the observation of the three-dimensional effect of particle motion on plasma filament dynamics in the electrostatic 3D-PIC simulation and have shown that the toroidal dependence of the dynamics arises from the electric field (potential) structure in a filament. As the ion temperature increases beyond the electron temperature, that is, the ion Larmor radius becomes larger than $\rho_e\sqrt{m_i/m_e}$, the toroidal gradient of the perpendicular electric field strength in a filament is extremely enhanced. This transformation of the electric field structure according to T_i provides the toroidal dependence to the filament dynamics.

As described in the previous works and this paper, the high ion temperature disturbs the radial transport of filaments through the poloidal symmetry breaking. In fusion boundary layer plasmas, this fact causes the modification of the total plasma transport in the high ion temperature plasma. Furthermore, as a consequence of the discovery presented in this paper, it will be necessary to consider the modification in the toroidal direction, i.e., according to the length from the end plate, for the exact prediction of the plasma transport.

In order to reveal the mechanism of the transformation of the electric field (potential) structure according to T_i, especially the large potential drop formation in the toroidal direction on the potential hill side in the high T_i cases, we need to analyze the particle dynamics in a filament in detail. On the other hand, Ref. 29 has shown that the blob spinning becomes important when the condition given by Eq. (29) in Ref. 29 is satisfied, i.e., the density in the main region is larger than that in the vicinity of the sheath. In the simulations shown in this paper, the initial density profile is uniform in the z direction. Thus, the condition given by Eq. (29) in Ref. 29 is not satisfied at the initial stage. However, after the simulation starts, the density in the vicinity of the end plates decreases than that in the main plasma. Furthermore, the decrease in the density around the end plates for the high T_i case is larger than that for the low T_i case. Therefore, the situation in which the condition for the importance of blob spinning is satisfied may occur in the high T_i case more easily than in the low T_i case. (Using the simulation parameters applied in this study, Eq. (29) in Ref. 29 becomes $n/n_{sh} \gtrsim 1.8$.) In future work, we will analyze the density dynamics along the magnetic field line and investigate the correlation between the parallel density dynamics and the filament propagation dynamics. Also, we plan to simulate the dynamics of the filament seeded three-dimensionally. In addition, it is important to study three-dimensional kinetic effects on filament dynamics with the atomic processes between plasma particles and neutral particles near conductive end plates by means of the PIC-MCC (PIC with Monte Carlo collision) code.[30]

ACKNOWLEDGMENTS

This work was performed on the "Plasma Simulator" of NIFS with the support and under the auspices of the NIFS Collaboration Research program (Nos. NIFS13KNSS038, NIFS15KNSS058, NIFS17KNSS086, NIFS17KNTS046, NIFS17KNTS049, and NIFS16KNTT038) and supported by JSPS KAKENHI Grant No. JP23740411.

REFERENCES

[1]M. Ryutova, *Physics of Magnetic Flux Tubes* (Springer-Verlag, Berlin and Heidelberg, 2015).
[2]S. I. Krasheninnikov, D. A. D'Ippolito, and J. R. Myra, J. Plasma Phys. **74**, 679 (2008).
[3]D. A. D'Ippolito, J. R. Myra, and S. J. Zweben, Phys. Plasmas **18**, 060501 (2011).
[4]J. A. Boedo, D. Rudakov, R. Moyer, S. Krasheninnikov, D. Whyte, G. McKee, G. Tynan, M. Schaffer, P. Stangeby, P. West, S. Allen, T. Evans, R. Fonck, E. Hollmann, A. Leonard, A. Mahdavi, G. Porter, M. Tillack, and G. Antar, Phys. Plasmas **8**, 4826 (2001).
[5]G. Y. Antar, G. Counsell, Y. Yu, B. Labombard, and P. Devynck, Phys. Plasmas **10**, 419 (2003).
[6]R. J. Maqueda, G. A. Wurden, S. Zweben, L. Roquemore, H. Kugel, D. Johnson, S. Kaye, S. Sabbagh, and R. Maingi, Rev. Sci. Instrum. **72**, 931 (2001).
[7]J. A. Boedo, D. L. Rudakov, R. A. Moyer, G. R. McKee, R. J. Colchin, M. J. Schaffer, P. G. Stangeby, W. P. West, S. L. Allen, T. E. Evans, R. J. Fonck, E. M. Hollmann, S. Krasheninnikov, A. W. Leonard, W. Nevins, M. A. Mahdavi, G. D. Porter, G. R. Tynan, D. G. Whyte, and X. Xu, Phys. Plasmas **10**, 1670 (2003).
[8]H. Tanaka, N. Ohno, Y. Tsuji, S. Kajita, S. Masuzaki, M. Kobayashi, T. Morisaki, H. Tsuchiya, A. Komori, and LHD Experimental Group, Phys. Plasmas **17**, 102509 (2010).
[9]E. de la Cal, P. Semwal, A. M. Aguilera, B. van Milligen, J. L. de Pablos, Z. Khan, and C. Hidalgo, Plasma Phys. Controlled Fusion **56**, 105003 (2014).
[10]D. A. D'Ippolito, J. R. Myra, and S. I. Krasheninnikov, Phys. Plasmas **9**, 222 (2002).
[11]S. Sugita, M. Yagi, S.-I. Itoh, and K. Itoh, J. Phys. Soc. Jpn. **79**, 044502 (2010).
[12]T. Maeda, K. Tominaga, S. Yamoto, A. Hatayama, H. Hasegawa, and S. Ishiguro, Contrib. Plasma Phys. **58**, 505 (2018).
[13]D. Jovanović, P. K. Shukla, and F. Pegoraro, Phys. Plasmas **15**, 112305 (2008).
[14]J. Madsen, O. E. Garcia, J. S. Larsen, V. Naulin, A. H. Nielsen, and J. J. Rasmussen, Phys. Plasmas **18**, 112504 (2011).
[15]N. Bisai and P. K. Kaw, Phys. Plasmas **20**, 042509 (2013).
[16]M. Wiesenberger, J. Madsen, and A. Kendl, Phys. Plasmas **21**, 092301 (2014).
[17]M. Held, M. Wiesenberger, J. Madsen, and A. Kendl, Nucl. Fusion **56**, 126005 (2016).
[18]P. Manz, G. Birkenmeier, D. Carralero, G. Fuchert, H. W. Müller, S. H. Müller, B. D. Scott, U. Stroth, T. T. Ribeiro, E. Wolfrum, and ASDEX Upgrade Team, Plasma Phys. Controlled Fusion **57**, 014012 (2015).
[19]P. W. Gingell, S. C. Chapman, R. O. Dendy, and C. S. Brady, Plasma Phys. Controlled Fusion **54**, 065005 (2012).
[20]H. Hasegawa and S. Ishiguro, Plasma **1**, 61 (2018).
[21]S. Ishiguro and H. Hasegawa, J. Plasma Phys. **72**, 1233 (2006).
[22]H. Hasegawa and S. Ishiguro, Plasma Fusion Res. **7**, 2401060 (2012).
[23]H. Hasegawa and S. Ishiguro, Plasma Fusion Res. **12**, 1401044 (2017).
[24]H. Hasegawa and S. Ishiguro, Phys. Plasmas **22**, 102113 (2015).
[25]H. Hasegawa and S. Ishiguro, Nucl. Fusion **57**, 116008 (2017).
[26]H. Hasegawa and S. Ishiguro, Nucl. Mater. Energy **19**, 473 (2019).
[27]C. K. Birdsall and A. B. Langdon, *Plasma Physics via Computer Simulation* (McGraw-Hill Book Company/Institute of Physics Publishing; Adam Hilger, New York; Bristol and Philadelphia; Bristol; and New York, 1985; 1991; 1991).
[28]J. R. Myra, D. A. Russell, and D. A. D'Ippolito, Phys. Plasmas **13**, 112502 (2006).
[29]J. R. Angus, S. I. Krasheninnikov, and M. V. Umansky, Phys. Plasmas **19**, 082312 (2012).
[30]T. Pianpanit, S. Ishiguro, and H. Hasegawa, Plasma Fusion Res. **11**, 2403040 (2016).